Atmos. Meas. Tech., 8, 2737–2748, 2015
www.atmos-meas-tech.net/8/2737/2015/
doi:10.5194/amt-8-2737-2015

Atmospheric Measurement Techniques
Open Access

Efficient photochemical generation of peroxycarboxylic nitric anhydrides with ultraviolet light-emitting diodes

N. D. Rider[1], Y. M. Taha[1], C. A. Odame-Ankrah[1], J. A. Huo[1], T. W. Tokarek[1], E. Cairns[1], S. G. Moussa[2], J. Liggio[2], and H. D. Osthoff[1]

[1]Department of Chemistry, University of Calgary, 2500 University Drive NW, Calgary, AB T2N 1N4, Canada
[2]Environment Canada, Air Quality Research Division, 4905 Dufferin Street, Toronto, Ontario, M3H 5T4, Canada

Correspondence to: H. D. Osthoff (hosthoff@ucalgary.ca)

Received: 24 December 2014 – Published in Atmos. Meas. Tech. Discuss.: 26 January 2015
Revised: 28 May 2015 – Accepted: 09 June 2015 – Published: 08 July 2015

Abstract. Photochemical sources of peroxycarboxylic nitric anhydrides (PANs) are utilized in many atmospheric measurement techniques for calibration or to deliver an internal standard. Conventionally, such sources rely on phosphor-coated low-pressure mercury (Hg) lamps to generate the UV light necessary to photo-dissociate a dialkyl ketone (usually acetone) in the presence of a calibrated amount of nitric oxide (NO) and oxygen (O_2). In this manuscript, a photochemical PAN source in which the Hg lamp has been replaced by arrays of ultraviolet light-emitting diodes (UV-LEDs) is described. The output of the UV-LED source was analyzed by gas chromatography (PAN-GC) and thermal dissociation cavity ring-down spectroscopy (TD-CRDS). Using acetone, diethyl ketone (DIEK), diisopropyl ketone (DIPK), or di-n-propyl ketone (DNPK), respectively, the source produces peroxyacetic (PAN), peroxypropionic (PPN), peroxyisobutanoic (PiBN), or peroxy-n-butanoic nitric anhydride (PnBN) from NO in high yield (> 90 %). Box model simulations with a subset of the Master Chemical Mechanism (MCM) were carried out to rationalize product yields and to identify side products. The present work demonstrates that UV-LED arrays are a viable alternative to current Hg lamp setups.

1 Introduction

The peroxycarboxylic nitric anhydrides (PANs, molecular formula $RC(O)O_2NO_2$) have long been recognized as important trace gas constituents of the troposphere (e.g., Darley et al., 1963; Singh and Hanst, 1981; Roberts, 1990, 2007). A crucial aspect in their measurement, for example, by gas chromatography with electron capture detection (PAN-GC) or by chemical ionization mass spectrometry (CIMS) (Flocke et al., 2005; Slusher et al., 2004; Zheng et al., 2011), is the generation of a stable and sufficiently pure standard in a gas stream for either instrument calibration or as an internal standard to track the effects of the sample matrix on the instrument response. Diffusion standards are often used for this purpose, but require challenging syntheses and storage in a non-polar solvent at water-ice (or colder) temperatures since PANs are prone to thermal decomposition and explosive in pure form. In addition, the output of diffusion sources is difficult to stabilize. A complicating factor is that the instrument response factors usually differ for each of the PAN species, such that several PAN species need to be synthesized. Hence, the deployment of diffusion standards has practical limitations in field campaign settings.

Photochemical sources that generate PANs in situ are an attractive alternative as they remove the need to transport, store, and dispose of liquid toxic chemicals and more readily provide a stable output. Most commonly, the PAN species most abundant in the atmosphere, peroxyacetic nitric anhydride (PAN), is produced from irradiation of acetone in its $n \rightarrow \pi^*$ band in the presence of a calibrated amount of NO in excess O_2 (Meyrahn et al., 1987; Warneck and Zerbach, 1992) by the following reaction sequence (for acetone, $R = CH_3$):

$$RC(O)R + h\nu \rightarrow RC(O) + R \quad \text{(R1)}$$

$$RC(O) + O_2 \rightarrow RC(O)O_2 \quad \text{(R2)}$$

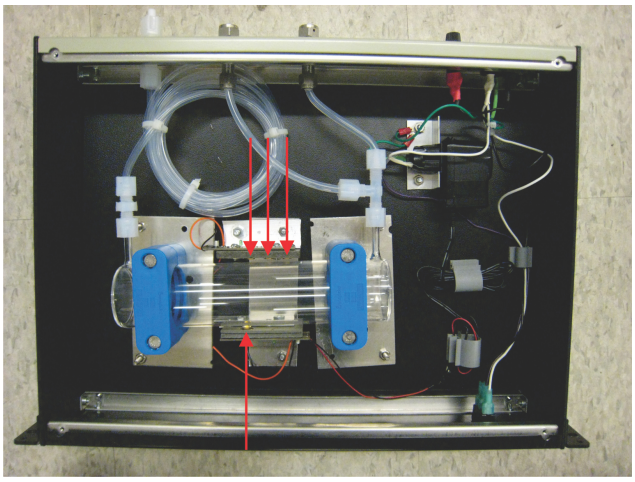

Figure 1. Photograph of the UV-LED photochemical source. The red arrows indicate the position of the LEDs.

$$R + O_2 \rightarrow RO_2 \quad \text{(R3)}$$

$$NO + RC(O)O_2 \rightarrow NO_2 + R + CO_2 \quad \text{(R4)}$$

$$NO + RO_2 \rightarrow NO_2 + RO \quad \text{(R5a)}$$

$$RC(O)O_2 + NO_2 \rightleftharpoons RC(O)O_2NO_2 \quad \text{(R6)}$$

Since the conversion of NO to PAN is reproducible and nearly quantitative (typically 95 %), the output of such a photochemical source is often directly calibrated using a conventional total odd nitrogen (NO_y) chemiluminescence (CL) analyzer or relative to the amount of NO delivered from a calibrated gas cylinder (Pätz et al., 2002; Volz-Thomas et al., 2002; Flocke et al., 2005).

It is also possible to generate other PAN species photochemically, for example, peroxypropionic nitric anhydride (PPN) from propanal and NO, a reaction which has been reported to proceed in quantitative yield with respect to NO (Volz-Thomas et al., 2002). Recently, Furgeson et al. (2011) demonstrated that PPN and peroxyisobutyric nitric anhydride (PiBN) can be generated from either NO or NO_2 and diethyl ketone (DIEK) or diisopropyl ketone (DIPK), respectively, with yields in the 70–90 % range. However, it has remained unclear if this method is suitable for calibration of the most commonly used PAN measurement technique, PAN-GC, in part because Volz-Thomas et al. (2002) had concluded it was not, but also because Furgeson et al. (2011) did not have access to a PAN-GC to show otherwise.

Conventionally, photochemical sources utilize compact low-pressure Hg lamps to generate UV light. For ketone photolysis, the Hg lamps are usually phosphor-coated to redshift the output from 254 to 285 nm. This minimizes generation of undesirable nitrogen oxide containing side products (i.e., alkyl nitrates and nitric acid) which interfere with calibration against NO_y CL (Flocke et al., 2005). However, the use of these lamps has several drawbacks: for one, they generate heat, which necessitates the use of a fan to avoid thermal decomposition of the desired PAN product. Furthermore, there is the risk of breakage and exposure of the operator to toxic Hg vapor.

During the construction of a photochemical PAN source, Furgeson et al. (2011) observed that several newly purchased phosphor-coated Hg lamps, contrary to manufacturer specifications, emitted residual radiation at 254 nm, which they suppressed by switching from a UV-transparent quartz photochemical cell to one constructed from Pyrex (which does not transmit UV-C light). The use of the Pyrex cell resulted in a high purity output but also a reduced overall yield as the Pyrex walls attenuated the desired 285 nm radiation. The PAN output of this source sufficed to produce a ^{13}C-labeled internal standard for a thermal dissociation chemical ionization mass spectrometer (TD-CIMS) in a mildly polluted environment (Mielke and Osthoff, 2012) but was insufficient in the more polluted conditions encountered during the Calnex-LA campaign (Mielke et al., 2013) and in Abbotsford, B.C. (Tokarek et al., 2014) motivating an improvement of the design of the photochemical source.

In this manuscript, we describe a second-generation photochemical PAN source in which the Hg lamp has been replaced by arrays of ultraviolet light-emitting diodes (UV-LEDs). The new photochemical source was used to generate PAN, PPN, PiBN, and peroxy-n-butanoic nitric anhydride (PnBN) from NO in O_2 and acetone, DIEK, DIPK, or di-n-propylketone (DNPK), respectively. The source output was quantified using a recently assembled PAN-GC (Tokarek et al., 2014) and by a thermal-dissociation cavity ring-down spectrometer (Paul and Osthoff, 2010). Box model simulations using a modified subset of the Master Chemical Mechanism (Jenkin et al., 1997; Saunders et al., 2003; Jenkin et al., 2012) were carried out to rationalize the observed yields of PAN, PPN and PiBN and to identify side products. The performance of the UV-LED photochemical source was compared to the earlier generation photochemical source equipped with a conventional phosphor-coated Hg lamp and Pyrex reactor.

2 Methods

2.1 UV-LED photochemical source

A photograph of the new UV-LED photochemical source is shown in Fig. 1. At the center, it contains a cylindrical quartz reaction chamber with the following dimen-

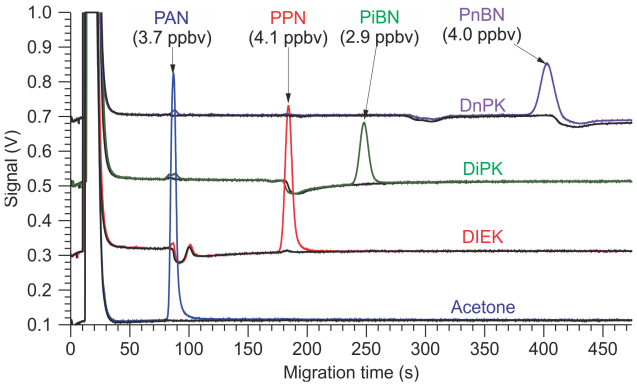

Figure 2. Sample chromatograms of PAN (blue trace), PPN (red trace), PiBN (green trace), and PnBN (purple trace) generated using the UV-LED photochemical source, 4.1 ppbv of NO, and acetone, DIEK, DIPK, and DNPK, respectively. The black traces show the respective chromatograms before the UV-LEDs were switched on. The chromatograms were vertically offset for clarity.

sions: length = 22.3 cm, outer diameter (o.d.) = 4.9 cm, internal volume = 450.5 cm^3, and wall thickness = 0.1 cm. The chamber was mounted inside a 19″ width, rack mount metal case but could have readily been mounted in a smaller enclosure if that had been desired. UV-LEDs were selected for best overlap with the ($n \rightarrow \pi^*$) band of the ketones (see Fig. 2 of Furgeson et al., 2011); the LEDs chosen in this work (Thorlabs LED285W) have a manufacturer-specified center wavelength of 285 ± 5 nm, a full-width at half-maximum (FWHM) of 12 nm, and typical optical power of 0.80 mW. The UV-LEDs were mounted on two arrays, which were designed and constructed in-house (Fig. S1 in the Supplement). Each array has the capacity to hold three UV-LEDs and contains a LT3465 LED driver integrated circuit to ensure a regulated constant current flow through each of the LEDs. Four LEDs were installed for the work presented here, drawing a combined total of 1.7 W of electrical power (for comparison, the two Hg lamp sources described by Furgeson et al. (2011) consume 51 and 58 W, respectively, half of which was required to operate the cooling fans). The diode arrays were mounted on opposite sides and in parallel to the reaction chamber (Fig. 1). Their optical output is quite divergent (manufacturer-specified half-viewing angle of 60°), and this configuration provided illumination over a wide area of the chamber ($\sim 1/2$) and removed the need to focus the LED outputs. Trials with quartz lenses did not produce higher PAN yields (data not shown).

Reagent gases were delivered in a similar fashion as described by Furgeson et al. (2011) and combined before entering the quartz chamber. The ketones were either delivered from a cylinder containing ^{13}C-labeled acetone (Scott-Marrin, 18.68 ppmv, balance zero air) or by passing O_2 (Praxair) through a three-valve glass trap as shown in Fig. 1 of Furgeson et al. (2011) containing liquid acetone, DIEK, DIPK, or DNPK (Sigma-Aldrich), which were used as received.

The gas stream containing the ketone was delivered at flow rates in the range of 10 to 50 standard cubic centimeters per minute (sccm) set using a 100 sccm capacity mass flow controller (MFC). NO (Scott-Marrin, 1.960 ppmv, balance N_2) was added at flow rates in the range from 0.2 to 12 sccm using an all-metal MFC . Under these conditions, residence times in the chamber ranged from 7 to 44 min (typically 15 min).

The gas mixture exiting the reaction chamber was passed through a 1 m long section of coiled 0.25″ o.d. Teflon tube to ensure that the source output contains a minimal amount of free radicals. The eluting mixture was then diluted with up to 6 standard L min^{-1} of zero air (Praxair) delivered by a third MFC and analyzed as described below.

2.2 Gas chromatography

Initial experiments were carried out using a Hewlett-Packard (HP) 5890 Series II gas chromatograph equipped with an ECD detector which was converted into a PAN-GC in a similar fashion as described by Fischer et al. (2010) and Tokarek et al. (2014). Briefly, the instrument was equipped with a two-position sample valve (VICI Valco EHC10WE), which was automated using a 14-bit data acquisition module and Labview software, and a 2 mL sample loop constructed from polyether ether ketone tubing. The analytical column was a fused silica mega-bore capillary (Restek RTX 1701, length 13.2 m, 0.25 µm coating thickness). The carrier gas was ECD-grade Helium (Praxair) which was purified with the aid of a "triple trap" (Restek 22473) and re-humidified using copper sulfate pentahydrate (Aldrich) for reasons outlined by Flocke et al. (2005). The carrier gas flow rate was 18 mL min^{-1}. Ultrapure N_2 (Praxair, ECD grade) was used as the make-up gas at a flow rate of 22 mL min^{-1} (which was optimized to give the lowest background counts). The ECD and GC oven were operated at temperatures of 30 and 27 °C, respectively. Both temperatures were deliberately set to above room temperature to avoid fluctuations in ECD response factors and column elution times. Peak fitting and data reduction were as described by Tokarek et al. (2014). Some experiments were replicated using the group's Varian PAN-GC whose construction and operation have been described by Tokarek et al. (2014) because the HP-GC had been modified for unrelated experiments.

2.3 Thermal dissociation cavity ring-down spectroscopy

The blue diode laser TD-CRDS used in this work was a modified version of the instrument described by Paul and Osthoff (2010). Briefly, NO_2 was measured via its optical absorption at 405 nm in an ambient temperature detection channel. Total peroxycarboxylic nitric anhydrates nitrates (ΣPN) were dissociated to NO_2 in a heated detection channel at an

inlet temperature of 250 °C (Day et al., 2002; Paul et al., 2009; Paul and Osthoff, 2010; Wooldridge et al., 2010) and quantified by difference. A recently added detection channel served to quantify NO_x ($=NO + NO_2$) through addition of excess O_3, which titrates NO to NO_2, and hence allowed NO mixing ratios to be calculated by subtraction (Fuchs et al., 2009). For the subtraction, it was assumed that the response to NO_2 was equal in all channels; in practice, the response varied somewhat between channels (because of, for example, differences in the purge flows protecting the ring-down mirrors), which limited the accuracy of the yields (presented in Sect. 3.2) to ± 5 % in this work.

DIEK gave rise to an offset in all CRDS channels equivalent to ∼ 2.0 ppbv of NO_2 and which varied on a time scale of hours. This offset was larger than had been observed in the earlier experiments by Furgeson et al. (2011) and could be lowered to ∼ 0.2 ppbv by cooling the trap in an ice-water bath and partially bypassing the oxygen flow, indicating that the offset was mainly due to an impurity in the reagent. An offset was observed with DIPK and DNPK as well, equivalent to ∼ 0.4 ppbv of NO_2. This offset could be lowered to ∼ 60 pptv when the trap was cooled in an ice-water bath. Since the magnitudes of these offsets were the same in all CRDS channels, the differences, i.e., the NO and ΣPN mixing ratios crucial to the work presented here, remained usable for quantification.

2.4 Box modeling

A box model was constructed from a subset of the MCM V3.2 obtained from http://mcm.leeds.ac.uk/MCM and run using the Atchem on-line tool V1.5 (Jenkin et al., 1997, 2012; Saunders et al., 2003) to simulate the production of PAN, PPN, and PiBN and side products, such as ethyl nitrate production during DIEK photolysis (Volz-Thomas et al., 2002), in the photochemical source. The mechanism was modified as described below and included as a Supplement.

The MCM contains the chemistry of DIEK and its degradation products, but neither DNPK nor DIPK are part of the MCM V3.2. The photo-dissociation of DIPK was added by using ethyl isopropyl ketone (EIPK) in its place and modifying the photo-products to isopropylperoxy and peroxyisobutyryl radical, i.e., $(CH_3)_2CHCO_2$ and $(CH_3)_2CHC(O)O_2$. In the MCM, the thermal decomposition rate of PiBN defaults to that of PAN; in this work, it was set to that of PPN, which is slower and more in line with recent experimental work (Kabir et al., 2014). In addition, the yield of methyl nitrate (CH_3ONO_2) in the reaction between the methylperoxy radical (CH_3O_2) and NO was increased from 0.1 to 1 % (Williams et al., 2014). Other studies (e.g., Scholtens et al., 1999) have reported a lower yield in the CH_3ONO_2 branching channel, but the larger value is used here as a precaution. Finally, photolysis reactions for PAN, PPN, PiBN and HO_2NO_2 were added. Heterogeneous reactions and wall losses of reactive radical species (i.e., OH) and acids (i.e., HONO and HNO_3) were not accounted for in this mechanism.

Photolysis frequencies were calculated using cross-sections and quantum yields recommended by the NASA-JPL (Jet Propulsion Laboratory) evaluation (Sander et al., 2010). The irradiance was estimated from the manufacturer-specified LED emission profile (which was assumed to be Gaussian) and combined output power of 4.8 mW; at the center of 285 nm, the irradiance was $\sim 0.1\,W\,m^{-2}\,nm^{-1}$. Simulations were initiated using 1.5×10^{11} molecules cm^{-3} of NO and 1.5×10^{11} molecules cm^{-3} of the respective dialkyl ketone at 293 K and a water vapor mixing ratio of 10 ppmv. Yields of PPN were also investigated at temperatures of 300, 311, and 323 K (for comparison with Fig. 5 of Volz-Thomas et al., 2002) and with water mixing ratios of 0.1 %.

The MCM does not include a side channel of the reaction of alkionyl radicals, RC(O), with molecular oxygen which generates OH and is a minor pathway at atmospheric pressure and 293 K (Blitz et al., 2002; Romero et al., 2005). An additional set of model simulations was performed that included this side channel (with OH yields of ∼ 3.5 % for $CH_3C(O) + O_2$ and ∼ 5.3 % for $C_2H_5C(O) + O_2$ and i-$C_3H_7C(O) + O_2$, respectively) and was compared to the simulations described above.

2.5 Diffusion standards

PAN, PPN, and PiBN were synthesized as described by Mielke and Osthoff (2012). Ethyl and n-propyl nitrate were synthesized from the reaction of dinitrogen pentoxide (N_2O_5) with a corresponding alcohol following the method of Kames et al. (1993), and i-propyl and i-butyl nitrate were purchased from Sigma-Aldrich and used as received.

3 Results

3.1 Gas chromatograms

Sample gas chromatograms (acquired with the Varian PAN-GC) of the photochemical source output are shown in Fig. 2. The same amount of NO (∼ 4.1 ppbv) was added in each experiment. The acetone, DIEK, and DIPK glass traps were cooled in a water-ice bath and partially bypassed to reduce the amount of ketone delivered.

Shown in black color are chromatograms of the source output before the UV-LEDs were switched on. DIEK, DIPK, and DNPK eluted as negative peaks at 95, 190, and 426 s, respectively. In addition, the chromatogram of DIEK contained two impurity peaks at 90 s and 102 s, that of DIPK an impurity eluting at 84 s, and that of DNPK a second negative peak at 302 s. These peaks were more pronounced when the bypass of the glass trap was closed and a larger ketone concentration was delivered (data not shown).

After the UV-LEDs were turned on, a single, large Gaussian-shaped peak appeared in each of the chromatograms as the respective major product. The elution times

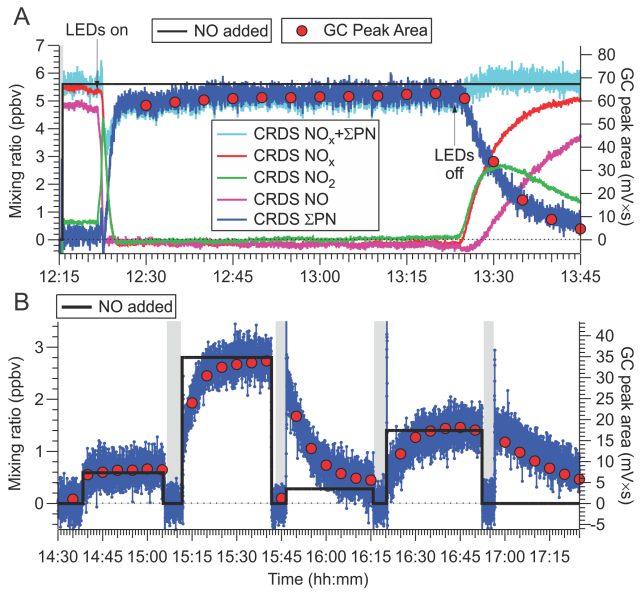

Figure 3. (a) Example of photochemical conversion of NO to PPN. Time series of NO (magenta), NO_2 (green), ΣPN (blue), NO_x (red), and $NO_x + \Sigma PN$ (turquoise) mixing ratios observed by TD-CRDS (1 s data presented) and of HP PAN-GC peak area (red circles) when the photochemical source was operated with DIEK to generate PPN. The black line is the NO mixing ratio (left axis) added to the UV-LED photo source, calculated from gas cylinder concentration and flow rates. An offset of 2.0 ppbv arising from DIEK was subtracted from the NO_2 and NO_x data prior to presentation. **(b)** Time series in which the amount of NO added was systematically varied as indicated by the black trace.

of these peaks were approximately 86, 188, 246, and 403 s, respectively, and consistent with those observed with diffusion standards and the relative elution times reported by Tanimoto et al. (1999), who had also used a RTX-1701 column to separate PANs. The ΣPN mixing ratios (shown as labels on the graph) indicate nearly quantitative conversion of NO to the respective peroxyacyl nitrate, with exception of PiBN. Here, the remainder appeared as NO_2, which suggests that PiBN production was limited by the production of peroxyisopropionyl radical in this particular experiment.

No impurity peaks were observed in the chromatogram generated from acetone. Additional features appeared in the chromatograms of the other compounds upon photolysis, however: with DIEK (red trace), the peak at 90 s increased slightly in height; this peak's retention time is consistent with PAN. There was no evidence of ethyl nitrate (which elutes about halfway between the oxygen peak and PAN). With DIPK (green trace), two small peaks were observed at 84 and 90 s (combined area ∼ 17 % that of PiBN). The first peak is likely due to isopropyl nitrate. The second peak's retention time is consistent with that of PAN. With DNPK, peaks appeared at 90 s (PAN) and 188 s (PPN) with a combined area ∼ 3 % that of PnBN, and the reagent peaks at 302 and 426 s decreased in height.

3.2 NO to PAN, PPN, PiBN and PnBN conversion efficiency

A time series of the CRDS NO (shown in magenta), NO_2 (green), NO_x (=NO+NO_2, red), ΣPN (blue), and $NO_x + \Sigma PN$ (turquoise) mixing ratios while the photochemical source was operated with DIEK to generate PPN is shown in Fig. 3a. Superimposed as red circles are the PPN peak areas observed by the HP PAN-GC. The black trace shows the delivered amount of NO, calculated using the gas cylinder concentration and gas flows (estimated accuracy ± 10 %). Between 12:15 and 12:21, the instruments sampled the output of the photochemical source with its UV light off. A small fraction of the NO had already oxidized (in the dark) to NO_2, likely due to the 2nd-order auto-oxidation of NO in the presence of O_2. At 12:21, the UV-LEDs were switched on. Full oxidation of NO was marked by its disappearance, the transient appearance of NO_2, and the appearance of PPN. The ΣPN mixing ratio was slightly lower (93.9 %) than the mixing ratio of NO_x observed earlier (and after the LED had been turned off), indicating that NO converted in nearly quantitative yield to PPN. At 13:22, the UV-LEDs were switched off, PPN disappeared, and NO_2 and NO reappeared, respectively.

Fig. 3b shows a time series in which the amount of NO reagent was deliberately varied. In addition, the output of the photochemical source was occasionally bypassed (gray underlay) to "zero" the instruments. In this experiment, the amount of PPN generated scaled directly with the amount of NO added, such that NO acted as the limiting reagent. When the amount of NO added was changed, the response was delayed as a result of the relatively slow flow rates through the reaction chamber. However, the TD-CRDS and PAN-GC signals were sufficiently correlated such that linear calibration plots could be generated from these data (see Sect. 3.4).

In experiments similar to the one described above (not shown), conversion of NO in acetone to PAN was observed to be quantitative within TD-CRDS measurement error (± 5 %). The yields of PiBN and PnBN (measured as ΣPN) relative to the amount of NO_x observed by TD-CRDS prior to photolysis were as high as (96 ± 5) % and (97 ± 5) %, respectively. The yields were lower when production was limited by the rate of peroxyacyl radical production (i.e., ketone concentration) as shown for PiBN in Fig. 2. Yields were also lower when the source was operated at a warmer temperature.

3.3 Comparison of UV-LED with Hg lamp photochemical source

The performance of the UV-LED photochemical source was compared to the photochemical source containing

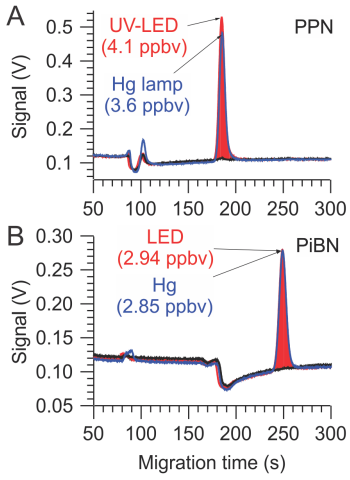

Figure 4. Comparison of UV-LED and Hg lamp output of **(a)** PPN and **(b)** PiBN.

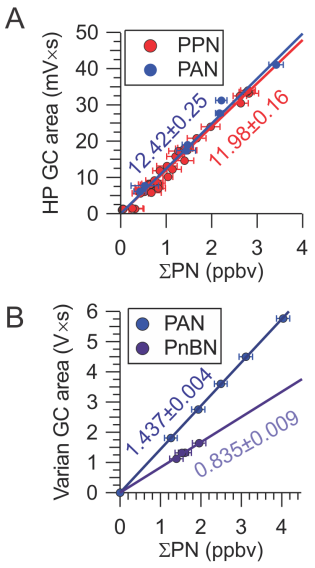

Figure 5. Sample calibration plots of PAN-GC peak area against ΣPN mixing ratio. **(a)** PAN and PPN as observed the HP PAN-GC. **(b)** PAN and PnBN as observed by the Varian PAN-GC.

a phosphor-coated Hg lamp described by Furgeson et al. (2011). A comparison of PPN and PiBN production is shown in Fig. 4. Both sources convert approximately the same amount of NO to PPN or PiBN, with no statistically significant difference in yield and impurity peak areas.

3.4 Sample calibration plots

Sample calibration plots of HP PAN-GC peak areas against ΣPN for PAN and PPN are shown in Fig. 5a, and sample calibration plots of Varian PAN-GC peak areas for PAN and PnBN are shown in Fig. 5b. In these experiments, the mixing ratio of NO delivered was systematically varied to change the ΣPN output. ΣPN mixing ratios were averaged over 20 s prior to the time of the PAN-GC injection. Data above mixing ratios of 10 ppbv were not used in these plots as the TD-CRDS response is non-linear above this mixing ratio (Paul et al., 2009; Paul and Osthoff, 2010). The data shown in Fig. 5 were each collected on the same day, as PAN-GC response factors varied between days (as the flows were turned down in the evenings to conserve gas and reset in the mornings).

For the HP PAN-GC, the slopes (in units of $\mathrm{mV \times s \times ppbv^{-1}}$) of these calibration curves were 12.42 ± 0.25 ($r = 0.997$) for PAN and 11.98 ± 0.16 ($r = 0.992$) for PPN, respectively. The PAN and PPN response factors were identical to those obtained with diffusion standards, and the relative responses of PAN : PPN of $1 : (0.965 \pm 0.023)$ are consistent with recent results in the literature (e.g., Flocke et al., 2005; Tokarek et al., 2014).

For the Varian PAN-GC, the slopes (in units of $\mathrm{V \times s \times ppbv^{-1}}$) were 1.437 ± 0.004 ($r = 0.9999$) for PAN and 0.835 ± 0.009 ($r = 0.9988$) for PnBN; i.e., the relative response of PAN : PnBN was $1 : (0.585 \pm 0.007)$.

3.5 Box model simulations

Figure 6 shows the results of the box model simulations. Table 1 summarizes the ratios (relative to NO_y) at the end of each simulation run. In all three cases, the desired peroxycarboxylic nitric anhydride is predicted as the major nitrogen oxide product (> 93 %), consistent with experiment.

Stable side products include the expected alkyl nitrates CH_3ONO_2, $C_2H_5ONO_2$ and i-$C_3H_7ONO_2$ in 0.32 %, 0.23 %, and 1.14 % yield, respectively. Alkyl nitrates are produced in the minor channel of the reaction between alkylperoxy radicals (RO_2) with NO:

$$\mathrm{NO + RO_2 \rightarrow RONO_2.} \qquad \text{(R5b)}$$

The time series indicates that this reaction occurs mainly in the initial phase before the NO has been oxidized (Fig. 6). The branching ratio of Reaction (R5b) relative to (R5a)–(R5b) increases with the number of carbons in the organic fragment *R* (Lightfoot et al., 1992; Perring et al., 2013); consequently, the yield of isopropyl nitrate (1.1 %) is greater than that of ethyl (0.2 %) and methyl nitrate (0.3 % – see Table 1). The latter is likely an upper limit because the relatively high yield by Williams et al. (2014) was used in the simulation.

With DIEK and DIPK, $C_2H_5C(O)CH_2CH_2ONO_2$ and $C_3H_7C(O)CH(CH_3)CH_2ONO_2$ are formed from reaction of DIEK or DIPK with OH (and subsequent reaction with NO_2) in 0.52 % and 0.66 % yield, respectively. The latter alkyl nitrates are not expected to elute on the time scale of the chromatograms shown in Fig. 2. The reaction sequence for this chemistry (shown for DIEK below) starts with abstraction of the terminal hydrogen of the ketone by OH followed by

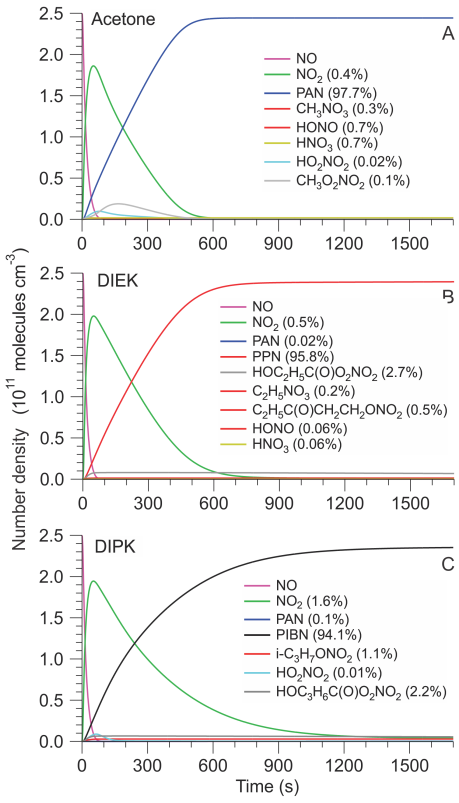

Figure 6. MCM box model simulations with different dialkyl ketones as starting material: **(a)** Acetone. **(b)** Diethyl ketone (DIEK). **(c)** Diisopropyl ketone (DIPK).

(rapid) production of the peroxy radical, which produces the alkyl nitrate via Reaction (R5b).

$$C_2H_5C(O)CH_2CH_3 + OH \rightarrow H_2O + C_2H_5C(O)CH_2CH_2 \quad (R7)$$

$$C_2H_5C(O)CH_2CH_2 + O_2 \rightarrow C_2H_5C(O)CH_2CH_2O_2 \quad (R8)$$

The OH radical comes from multiple sources, including photolysis of O_3 (produced from NO_2 photolysis and subsequent combination of the atomic with molecular oxygen) to O^1D and subsequent reaction with H_2O as well radical cycling with HO_2, produced, for example, from the reaction of alkoxy radicals (generated in Reaction R5a) with molecular oxygen.

Nitrous and nitric acid are negligible side products with DIEK and DIPK at yields of < 0.1 %, but are each produced from acetone with a yield of 0.7 %, respectively.

In the case of DIEK and DIPK, the model predicts formation of hydroxyl group bearing PANs (yield 2.74 and 2.23 % relatively to NO_y). These would likely elute well after PPN and PIBN and hence not interfere with the PAN-GC, but would systematically bias ΣPN high. They are produced from the peroxy radical produced in Reaction (R8), which can convert to the alcohol in a minor channel when reacting with RO_2:

$$C_2H_5C(O)CH_2CH_2O_2 + RO_2 \rightarrow C_2H_5C(O)CH_2CH_2OH + \text{other}. \quad (R9)$$

The alcohol is subject to photolysis and produces the hydroxygroup bearing PAN via Reactions (R1—R2) and (R6). However, it has been suggested (e.g., Zheng et al., 2011) that hydroxy-PANs such as β-hydroxyperoxyacetic nitric anhydride (HPAN) are unstable with respect to unimolecular decomposition, such that is unclear if their formation ultimately has any impact.

When the OH production rate is increased by including OH production from $RC(O) + O_2$ (Table 1, columns labeled with MCM*), the yields of the desired PAN products are marginally lowered, and the yield of alkyl nitrates decreases as well.

In all cases, NO_2 is predicted as a side product (yields at 293 K: 0.42, 0.54 and 1.60 %, respectively). To assess the yields of NO_2 and other products at higher operating temperatures (which may be encountered with a Hg lamp setup), additional simulations were carried out at 300, 311, and 323 K, respectively. Table 2 summarizes the results. More NO_2 and less PPN are produced as the temperature is increased, as expected. In contrast to results reported by Volz-Thomas et al. (2002), less ethyl nitrate is produced as the temperature is increased. The predicted product yields remained essentially unchanged (< 0.1 % difference) when the water mixing ratio was increased from 10 ppm to 0.1 % (data not shown).

The box model simulations also yield α,β-dicarbonyls, which interfere with the quantification of NO_2 by optical absorption in the TD-CRDS (Table 3). Acetone and diethyl ketone photolysis produce 244 pptv of methylglyoxal and 36 pptv of 2,3-pentadione, respectively, which increases to 440 and 192 pptv, respectively, after the OH generation from alkionyl radical plus molecular oxygen is included. The α,β-dicarbonyls are produced by abstraction of a hydrogen atom on the carbon adjacent to the carbonyl, for example, for DIEK:

$$C_2H_5C(O)CH_2CH_3 + OH \rightarrow C_2H_5C(O)CHCH_3 + H_2O. \quad (R10)$$

This radical converts to the peroxyradical by adding molecular oxygen (Reaction R3), which in turn reacts with NO to generate the alkoxy radical (Reaction R5). Subsequent H-abstraction produces the dicarbonyl:

$$C_2H_5C(O)CH(O)CH_3 + O_2 \rightarrow C_2H_5C(O)C(O)CH_3 + HO_2. \quad (R11)$$

Negligible amounts of $\alpha,\beta-$dicarbonyls are produced from DIPK photolysis, likely because abstraction of the hydrogen atom adjacent to the carbonyl group is more sterically hindered.

Table 1. Photo source product yields, relative to the amount of NO added, predicted by MCM box model simulations and observed. Species with an abundance of $< 5 \times 10^{-6}$ relative to NO_y are omitted. nd = below limit of detection.

	Acetone			DIEK			DIPK		
Species	MCM	MCM*	Expt.	MCM	MCM*	Expt.	MCM	MCM*	Expt.
PAN	97.7 %	97.6 %		0.02 %	0.06 %		0.11 %	0.11 %	
PPN	–	–		95.8 %	95.2 %		–	–	
PiBN	–	–		–	–		94.1 %	93.3 %	
$HOCH_2CH_2C(O)$-O_2NO_2	–	–		2.7 %	3.2 %		–	–	
$HOCH_2CH(CH_3)$-$C(O)O_2NO_2$	–	–		–	–		2.23 %	2.84 %	
ΣPN	97.7 %	97.6 %	(100 ± 5) %	98.6 %	98.5 %	(94 ± 5) %	96.4 %	96.3 %	(96 ± 5) %
CH_3ONO_2	0.32 %	0.32 %		–	–		–	–	
$C_2H_5ONO_2$	–	–		0.23 %	0.22 %		–	–	
i-$C_3H_7ONO_2$	–	–		–	–		1.14 %	1.13 %	
$C_2H_5C(O)CH_2$-CH_2ONO_2	–	–		0.52 %	0.53 %		–	–	
$HOCH_2CH_2ONO_2$	–	–		0.03 %	0.03 %		–	–	
$C_3H_7C(O)CH$-$(CH_3)CH_2ONO_2$	–	–		–	–		0.66 %	0.68 %	
$HOCH_2CH$-$(CH_3)ONO_2$	–	–		–	–		0.11 %	0.11 %	
ΣAN	0.32 %	0.32 %	nd	0.77 %	0.77 %	nd	1.91 %	1.92 %	nd
NO	–	–	nd	–	–	nd	–	–	nd
NO_2	0.43 %	0.42 %	nd	0.54 %	0.58 %	nd**	1.60 %	1.72 %	nd**
NO_3	–	–		–	–		–	–	
HONO	0.69 %	0.69 %		0.06 %	0.06 %		0.03 %	0.03 %	
HNO_3	0.73 %	0.82 %		0.06 %	0.08 %		0.03 %	0.04 %	
$CH_3O_2NO_2$	0.09 %	0.09 %		–	–		–	–	
HO_2NO_2	0.02 %	0.02 %		0.02 %	0.02 %		0.01 %	0.01 %	
Nitrate (NA)	0.01 %	0.01 %		0.00 %	0.00 %		0.00 %	0.00 %	
Σother	1.95 %	2.02 %		0.68 %	0.72 %		1.67 %	1.80 %	

* MCM simulation with the mechanism allowing for OH production from $RC(O) + O_2$.
** Measurement of NO_2 was compromised by an offset (see Sect. 2.3).

4 Discussion

4.1 Efficient photochemical production of PPN, PiBN, and PnBN

The photochemical production PAN from acetone observed in this work is consistent with literature (e.g., (Meyrahn et al., 1987; Warneck and Zerbach, 1992; Pätz et al., 2002; Volz-Thomas et al., 2002; Flocke et al., 2005) and hence does not require further discussion. Production of PPN, PiBN, and PnBN from DIEK, DIPK, and DNPK is less established (Furgeson et al., 2011) and has not been studied by PAN-GC or by MCM box modeling prior to this work.

The chromatograms in Fig. 2 show PPN, PiBN, and PnBN are indeed produced in high purity, consistent with box model results (Fig. 5) that show PPN and PiBN as the expected major photoproducts with yields > 90 %. This result is consistent with the work by Furgeson et al. (2011) but contradicts the earlier work by Volz-Thomas et al. (2002), who first evaluated generation of PPN from DIEK using a Hg lamp and presented a chromatogram similar to the one shown in Fig. 2. In their work, they identified a large impurity peak as ethyl nitrate. We also observed a peak at about the same relative retention time (∼ 102 s) which was present "in the dark", i.e., before the photochemical source was turned on. However, this retention time is inconsistent with ethyl nitrate, which we verified elutes much earlier, consistent with Roberts et al. (1989), and whose area was considerably reduced when we lowered the DIEK output from the trap. Further, ethyl nitrate is predicted only as a minor product in DIEK photolysis (Table 1). Because we observe nearly quantitative conversion of NO to PPN, the peak we observe at 102 s is most likely an impurity present in the DIEK reagent in our experiments. Regardless, with either the UV-LED or Hg lamp source, alkyl nitrate co-generation is at a negligible level.

The use of DIEK, DIPK, and DNPK has a disadvantage in that they give rise to negative peaks in the chromatograms. Apparently, the dialkyl ketones do not "capture" electrons in the ECD, but instead increase the current between the ECD's collector anode and cathode. Fortunately, these negative peaks are sufficiently separated from their respective PAN photoproducts. In the case of DNPK, multiple negative peaks suggest the presence of at least one ketone impurity in the DNPK sample.

The chromatograms in Fig. 2 show PAN as a very minor side product when DIEK, DIPK or DNPK were used. However, PAN was not observed in all experiments. We suspect that it arises because acetone was used to clean the glass trap between uses, or perhaps because acetone was present as a trace impurity in the reagents. Be it as it may, the interference from PAN in these experiments is negligibly small.

Table 2. Product yields of PPN and side products as a function of temperature predicted by box modeling.

	293 K	300 K	311 K	323 K
PPN	95.786 %	95.378 %	90.324 %	65.679 %
PAN	0.020 %	0.021 %	0.022 %	0.019 %
$HOCH_2CH_2C(O)O_2NO_2$	2.743 %	2.037 %	0.486 %	0.055 %
ΣPN	98.550 %	97.436 %	90.832 %	65.753 %
$C_2H_5ONO_2$	0.228 %	0.221 %	0.214 %	0.212 %
$C_2H_5C(O)CH_2CH_2ONO_2$	0.516 %	0.523 %	0.531 %	0.532 %
$HOCH_2CH_2ONO_2$	0.028 %	0.028 %	0.028 %	0.029 %
ΣAN	0.771 %	0.772 %	0.773 %	0.773 %
NO	1.1×10^{-7}	3.5×10^{-7}	1.8×10^{-6}	7.6×10^{-6}
NO_2	0.543 %	1.652 %	8.246 %	33.320 %
HONO	0.057 %	0.055 %	0.052 %	0.049 %
HNO_3	0.060 %	0.061 %	0.062 %	0.065 %
HO_2NO_2	0.017 %	0.023 %	0.033 %	0.037 %
Σother	0.677 %	1.791 %	8.393 %	33.473 %

Table 3. Yields of major α,β-dicarbonyls produced as byproducts in the photocell (in molecules cm^{-3} unless stated otherwise).

	Acetone		DIEK		DIPK	
Species	MCM	MCM*	MCM	MCM*	MCM	MCM*
Methylglyoxal	6.1×10^9	1.1×10^{10}	–	–	1.7×10^4	1.0×10^6
2,3-pentadione	–	–	9.1×10^8	4.8×10^9	1.8×10^5	4.7×10^6
Glyoxal	–	–	2.4×10^6	5.6×10^8	1.6×10^4	3.0×10^5
Sum	6.1×10^9	1.1×10^{10}	9.1×10^8	5.4×10^9	2.1×10^5	6.0×10^6
Sum (pptv)	244	440	36	214	0.0	0.2
Expected NO_2 interference (pptv)	24	44	4	23	–	–
Observed NO_2 interference (pptv)	below LOD		200		60	

* MCM simulation with the mechanism allowing for OH production from RC(O) + O_2.

4.2 Use of thermal dissociation methods with photochemical sources

The use of the photochemical sources gives rise to offsets in the CRDS absorption signals (Furgeson et al., 2011) which need to be taken into account when reducing the data. The species causing this offset mostly originate outside of the photochemical source, as the offset is there before the lights are turned on. Simple ketones do not significantly absorb at 405 nm (Martinez et al., 1992), but α,β-dicarbonyls do (Fuchs et al., 2009). We speculate that the interfering species are dialkyl diketones, generated mainly from dimerization of acyl radicals which are produced during ketone photolysis, and that these species are generated slowly in the reagent solutions. We were able to reduce, but not completely eliminate, these offsets by lowering the concentrations of the ketone and the impurities emitted with the aid of an ice bath. The MCM model simulations show that acetone and diethyl ketone photolysis produce several 100 pptv of methyl glyoxal (when acetone is used) and 2,3-pentadione (with DIEK), respectively. The 405 nm absorption cross-sections of α,β-dicarbonyls produced in the MCM simulations are each approximately an order of magnitude less than that of NO_2 (Szabo et al., 2011; Horowitz et al., 2001; Staffelbach et al., 1995; Paul and Osthoff, 2010). The observed offsets (Table 3, last row) are consistent with what was observed for acetone, but higher than predicted for DIEK and DIPK, for reasons that are unclear. The higher offsets suggest that either more than simulated OH was produced and/or that the yields of dicarbonyls in the MCM are underestimated. Fortunately, since ΣPN and NO were both determined by difference and the offset appeared to affect all CRDS channels equally, these offsets were of no further consequence in this work.

4.3 Utility of UV-LEDs: comparison with Hg lamps

The present work shows that the UV-LED photochemical source is a viable alternative to the commonly used Hg lamp

setup. The performance of the new UV-LED and the (previously optimized) Hg setups demonstrated in this manuscript were equal (Fig. 4), in part because the UV-LED source was not optimized for maximum output concentration. When a large excess of ketone was delivered by closing the bypass valve of the glass traps, mixing ratios in excess of 50 ppbv PPN could be generated from NO (data not shown). However, large ketone concentrations were not desirable in this work as they generated large negative peaks in the GC chromatograms and large positive offsets in the TD-CRDS signal.

In general, we found it easier to generate greater concentrations while maintaining a high purity output with the UV-LED source than our experiences have been with the Hg setup. There are multiple reasons for this, including a greater light output over a narrower wavelength range and minimal generation of heat. The narrower wavelength range of UV-LEDs is an advantage in that the UV-C radiation emitted by Hg lamps can lead to unwanted side reactions (e.g., PAN photolysis), whereas the output of the UV-LED maximizes ketone photo-dissociation. Hg lamps generate a considerable amount of heat, which is redistributed using a fan or blower; this, in closed environments, can still warm up the photochemical reaction chamber, which dissociates PANs to peroxyacyl radicals and NO_2 (Table 2). In contrast, UV-LEDs dissipate virtually no heat. Further, the low power consumption of the source may be useful in remote environments, where power can be scarce.

Another advantage of using UV-LEDs is design flexibility. Though the geometry of quartz reactor was not optimized in this work, the compact nature of the diodes provides flexibility to alter the chamber geometry and to incorporate this type of source in a tight space, which can be an important consideration in tight spaces during field deployments (e.g., on an aircraft). One possible design improvement is to use a hollow cylinder, with the LED arrays mounted inside, facing outward. This design would potentially allow for more efficient absorption of all photons emitted, in particular if the outside of the reactor were to be covered with a reflective coating.

Furthermore, the UV-LED setup has a low risk of breakage and long expected lifetime; in contrast, with a Hg lamp, there is always a risk of exposing the operator to toxic mercury vapor. At this point, we have insufficient data to tell if there are any significant differences to the conventional Hg lamp setup in terms of longevity, but this will be evaluated in future experiments.

The only disadvantage of the UV-LED setup is its price to construct; each of the UV-LEDs currently retails for about the same price as a phosphor-coated Hg lamp. There is also the added cost to construct the diode array driver circuits. At the same time, the ability to combine LEDs into arrays is an enormous advantage as the output of the source can be increased further simply by adding more diodes. With Hg lamps, that is in principle also possible but not practical considering the large heat load this would introduce.

4.4 Use of photochemical sources for calibration of PAN instruments

Overall, this work has demonstrated that it is possible to use dialkyl ketones to generate PAN, PPN, and PiBN in the same high yields and purity as reported for the acetaldehyde and propanal methods (Volz-Thomas et al., 2002). The source output sufficed to calibrate the two PAN-GCs against TD-CRDS with linear scatter plots.

The conversion of NO to the PAN products was sufficiently high such that the UV-LED photochemical source could have been used for calibration even if only a NO chemiluminescence measurement or a well calibrated NO delivery system had been on hand. However, because the PAN yield is dependent on temperature (Table 2), calibration of PAN on the basis of the amount of NO added alone may not be advisable in all field campaign settings.

The Supplement related to this article is available online at doi:10.5194/amt-8-2737-2015-supplement.

Acknowledgements. This work was supported by the Natural Science and Engineering Research Council of Canada (NSERC) in form of a Discovery grant (to H. D. Osthoff), a postdoctoral fellowship (to S. G. Moussa), two undergraduate student research awards (USRA, to N. D. Rider and J. A. Huo) and the CREATE program IACPES, which provided matching undergraduate student stipends (to N. D. Rider and J. A. Huo) and a graduate student scholarship (to Y. M. Taha). The authors thank the Open Access Authors Fund, Libraries and Cultural Resources, University of Calgary for covering the publication fees.

Edited by: G. Phillips

References

Blitz, M. A., Heard, D. E., and Pilling, M. J.: OH formation from $CH_3CO + O_2$: a convenient experimental marker for the acetyl radical, Chem. Phys. Lett., 365, 374–379, doi:10.1016/S0009-2614(02)01484-7 , 2002.

Darley, E. F., Kettner, K. A., and Stephens, E. R.: Analysis of Peroxyacyl Nitrates by Gas Chromatography with Electron Capture Detection, Anal. Chem., 35, 589–591, doi:10.1021/ac60197a028, 1963.

Day, D. A., Wooldridge, P. J., Dillon, M. B., Thornton, J. A., and Cohen, R. C.: A thermal dissociation laser-induced fluorescence instrument for in situ detection of NO_2, peroxy nitrates, alkyl nitrates, and HNO_3, J. Geophys. Res., 107, 4046, doi:10.1029/2001JD000779, 2002.

Fischer, E. V., Jaffe, D. A., Reidmiller, D. R., and Jaegle, L.: Meteorological controls on observed peroxyacetyl nitrate at Mount Bachelor during the spring of 2008, J. Geophys. Res., 115, D03302, doi:10.1029/2009JD012776, 2010.

Flocke, F. M., Weinheimer, A. J., Swanson, A. L., Roberts, J. M., Schmitt, R., and Shertz, S.: On the measurement of PANs by gas chromatography and electron capture detection, J. Atmos. Chem., 52, 19–43, doi:10.1007/s10874-005-6772-0, 2005.

Fuchs, H., Dubé, W. P., Lerner, B. M., Wagner, N. L., Williams, E. J., and Brown, S. S.: A Sensitive and Versatile Detector for Atmospheric NO_2 and NO_x Based on Blue Diode Laser Cavity Ring-Down Spectroscopy, Environ. Sci. Technol., 43, 7831–7836, doi:10.1021/es902067h, 2009.

Furgeson, A., Mielke, L. H., Paul, D., and Osthoff, H. D.: A photochemical source of peroxypropionic and peroxyisobutanoic nitric anhydride, Atmos. Environ., 45, 5025–5032, doi:10.1016/j.atmosenv.2011.03.072, 2011.

Horowitz, A., Meller, R., and Moortgat, G. K.: The UV-VIS absorption cross sections of the alpha-dicarbonyl compounds: Pyruvic acid, biacetyl and glyoxal, J. Photoch. Photobio. A, 146, 19–27, doi:10.1016/S1010-6030(01)00601-3 , 2001.

Jenkin, M. E., Saunders, S. M., and Pilling, M. J.: The tropospheric degradation of volatile organic compounds: a protocol for mechanism development, Atmos. Environ., 31, 81–104, doi:10.1016/S1352-2310(96)00105-7, 1997.

Jenkin, M. E., Wyche, K. P., Evans, C. J., Carr, T., Monks, P. S., Alfarra, M. R., Barley, M. H., McFiggans, G. B., Young, J. C., and Rickard, A. R.: Development and chamber evaluation of the MCM v3.2 degradation scheme for β-caryophyllene, Atmos. Chem. Phys., 12, 5275–5308, doi:10.5194/acp-12-5275-2012, 2012.

Kabir, M., Jagiella, S., and Zabel, F.: Thermal Stability of n-Acyl Peroxynitrates, Int. J. Chem. Kinet., 46, 462–469, doi:10.1002/kin.20862, 2014.

Kames, J., Schurath, U., Flocke, F., and Volzthomas, A.: Preparation of organic nitrates from alcohols and N_2O_5 for species identification in atmospheric samples, J. Atmos. Chem., 16, 349–359, doi:10.1007/BF01032630, 1993.

Lightfoot, P. D., Cox, R. A., Crowley, J. N., Destriau, M., Hayman, G. D., Jenkin, M. E., Moortgat, G. K., and Zabel, F.: Organic Peroxy-Radicals – Kinetics, Spectroscopy And Tropospheric Chemistry, Atmos. Environ. A, 26, 1805–1961, doi:10.1016/0960-1686(92)90423-I, 1992.

Martinez, R. D., Buitrago, A. A., Howell, N. W., Hearn, C. H., and Joens, J. A.: The near-UV absorption spectra of several aliphatic aldehydes and ketones at 300 K, Atmos. Environ. A-Gen., 26, 785–792, doi:10.1016/0960-1686(92)90238-G, 1992.

Meyrahn, H., Helas, G., and Warneck, P.: Gas-chromatographic determination of peroxyacyetyl nitrate – 2 convenient calibration techniques, J. Atmos. Chem., 5, 405–415, doi:10.1007/bf00113903, 1987.

Mielke, L. H. and Osthoff, H. D.: On quantitative measurements of peroxycarboxylic nitric anhydride mixing ratios by thermal dissociation chemical ionization mass spectrometry, Int. J. Mass Spectrom., 310, 1–9, doi:10.1016/j.ijms.2011.10.005, 2012.

Mielke, L. H., Stutz, J., Tsai, C., Hurlock, S. C., Roberts, J. M., Veres, P. R., Froyd, K. D., Hayes, P. L., Cubison, M. J., Jimenez, J. L., Washenfelder, R. A., Young, C. J., Gilman, J. B., de Gouw, J. A., Flynn, J. H., Grossberg, N., Lefer, B. L., Liu, J., Weber, R. J., and Osthoff, H. D.: Heterogeneous formation of nitryl chloride and its role as a nocturnal NO_x reservoir species during CalNex-LA 2010, J. Geophys. Res., 118, 10638–10652, doi:10.1002/jgrd.50783, 2013.

Pätz, H.-W., Lerner, A., Houben, N., and Volz-Thomas, A.: Validation of a new method for the calibration of peroxy acetyl nitrate (PAN)-analyzers, Gefahrst. Reinhalt. L., 62, 215–219, 2002.

Paul, D., Furgeson, A., and Osthoff, H. D.: Measurement of total alkyl and peroxy nitrates by thermal decomposition cavity ring-down spectroscopy, Rev. Sci. Instrum., 80, 114101, doi:10.1063/1.3258204 2009.

Paul, D. and Osthoff, H. D.: Absolute Measurements of Total Peroxy Nitrate Mixing Ratios by Thermal Dissociation Blue Diode Laser Cavity Ring-Down Spectroscopy, Anal. Chem., 82, 6695–6703, doi:10.1021/ac101441z, 2010.

Perring, A. E., Pusede, S. E., and Cohen, R. C.: An Observational Perspective on the Atmospheric Impacts of Alkyl and Multifunctional Nitrates on Ozone and Secondary Organic Aerosol, Chem. Rev., 113, 5848–5870, doi:10.1021/cr300520x, 2013.

Roberts, J. M., Fajer, R. W., and Springston, S. R.: Capillary gas chromatographic separation of alkyl nitrates and peroxycarboxylic nitric anhydrides, Anal. Chem., 61, 771–772, doi:10.1021/ac00182a026, 1989.

Roberts, J. M.: The atmospheric chemistry of organic nitrates, Atmos. Environ. A-Gen., 24, 243–287, doi:10.1016/0960-1686(90)90108-Y, 1990.

Roberts, J. M.: PAN and Related Compounds, in: Volatile Organic Compounds in the Atmosphere, edited by: Koppmann, R., Blackwell Publishing, Oxford, UK, 221–268, 2007.

Romero, M. T. B., Blitz, M. A., Heard, D. E., Pilling, M. J., Price, B., and Seakins, P. W.: OH formation from the $C_2H_5CO+O_2$ reaction: An experimental marker for the propionyl radical, Chem. Phys. Lett., 408, 232–236, doi:10.1016/j.cplett.2005.04.018, 2005.

Sander, S. P., Abbatt, J. P. D., Barker, J. R., Burkholder, J. B., Friedl, R. R., Golden, D. M., Huie, R. E., Kolb, C. E., Kurylo, M. J., Moortgat, G. K., Orkin, V. L., and Wine, P. H.: Chemical Kinetics and Photochemical Data for Use in Atmospheric Studies, Evaluation No. 17, JPL Publication 10-6, Jet Propulsion Laboratory, Pasadena, CA, 2010.

Saunders, S. M., Jenkin, M. E., Derwent, R. G., and Pilling, M. J.: Protocol for the development of the Master Chemical Mechanism, MCM v3 (Part A): tropospheric degradation of non-aromatic volatile organic compounds, Atmos. Chem. Phys., 3, 161–180, doi:10.5194/acp-3-161-2003, 2003.

Scholtens, K. W., Messer, B. M., Cappa, C. D., and Elrod, M. J.: Kinetics of the CH_3O_2+ NO Reaction: Temperature Dependence of the Overall Rate Constant and an Improved Upper Limit for the CH_3ONO_2 Branching Channel, J. Phys. Chem. A, 103, 4378–4384, doi:10.1021/jp990469k, 1999.

Singh, H. B. and Hanst, P. L.: Peroxyacetyl nitrate (PAN) in the unpolluted atmosphere – an important reservoir for nitrogen oxides, Geophys. Res. Lett., 8, 941–944, doi:10.1029/GL008i008p00941, 1981.

Slusher, D. L., Huey, L. G., Tanner, D. J., Flocke, F. M., and Roberts, J. M.: A thermal dissociation-chemical ionization mass spectrometry (TD-CIMS) technique for the simultaneous measurement of peroxyacyl nitrates and dinitrogen pentoxide, J. Geophys. Res., 109, D19315, doi:10.1029/2004JD004670, 2004.

Staffelbach, T. A., Orlando, J. J., Tyndall, G. S., and Calvert, J. G.: The UV-visible absorption spectrum and photolysis quantum yields of methylglyoxal, J. Geophys. Res.-Atmos., 100, 14189–14198, doi:10.1029/95jd00541, 1995.

Szabo, E., Djehiche, M., Riva, M., Fittschen, C., Coddeville, P., Sarzyński, D., Tomas, A., and Dóbé , S.: Atmospheric Chemistry of 2,3-Pentanedione: Photolysis and Reaction with OH Radicals, J. Phys. Chem. A, 115, 9160–9168, doi:10.1021/jp205595c, 2011.

Tanimoto, H., Hirokawa, J., Kajii, Y., and Akimoto, H.: A new measurement technique of peroxyacetyl nitrate at parts per trillion by volume levels: Gas chromatography/negative ion chemical ionization mass spectrometry, J. Geophys. Res., 104, 21343–21354, doi:10.1029/1999JD900345, 1999.

Tokarek, T. W., Huo, J. A., Odame-Ankrah, C. A., Hammoud, D., Taha, Y. M., and Osthoff, H. D.: A gas chromatograph for quantification of peroxycarboxylic nitric anhydrides calibrated by thermal dissociation cavity ring-down spectroscopy, Atmos. Meas. Tech., 7, 3263–3283, doi:10.5194/amt-7-3263-2014, 2014.

Volz-Thomas, A., Xueref, I., and Schmitt, R.: An automatic gas chromatograph and calibration system for ambient measurements of PAN and PPN, Environ. Sci. Pollut. R., 9, 72–76, 2002.

Warneck, P. and Zerbach, T.: Synthesis of peroxyacetyl nitrate in air by acetone photolysis, Environm. Sci. Technol., 26, 74–79, doi:10.1021/es00025a005, 1992.

Williams, J. E., Le Bras, G., Kukui, A., Ziereis, H., and Brenninkmeijer, C. A. M.: The impact of the chemical production of methyl nitrate from the $NO + CH_3O_2$ reaction on the global distributions of alkyl nitrates, nitrogen oxides and tropospheric ozone: a global modelling study, Atmos. Chem. Phys., 14, 2363–2382, doi:10.5194/acp-14-2363-2014, 2014.

Wooldridge, P. J., Perring, A. E., Bertram, T. H., Flocke, F. M., Roberts, J. M., Singh, H. B., Huey, L. G., Thornton, J. A., Wolfe, G. M., Murphy, J. G., Fry, J. L., Rollins, A. W., LaFranchi, B. W., and Cohen, R. C.: Total Peroxy Nitrates (ΣPNs) in the atmosphere: the Thermal Dissociation-Laser Induced Fluorescence (TD-LIF) technique and comparisons to speciated PAN measurements, Atmos. Meas. Tech., 3, 593–607, doi:10.5194/amt-3-593-2010, 2010.

Zheng, W., Flocke, F. M., Tyndall, G. S., Swanson, A., Orlando, J. J., Roberts, J. M., Huey, L. G., and Tanner, D. J.: Characterization of a thermal decomposition chemical ionization mass spectrometer for the measurement of peroxy acyl nitrates (PANs) in the atmosphere, Atmos. Chem. Phys., 11, 6529–6547, doi:10.5194/acp-11-6529-2011, 2011.